Cement and Concrete Research 144 (2021) 106402

Contents lists available at ScienceDirect

Cement and Concrete Research

journal homepage: www.elsevier.com/locate/cemconres

Shrinkage-induced deformations and creep of structural concrete: 1-year measurements and numerical prediction

Petr Havlásek [a,*], Vít Šmilauer [a], Lenka Dohnalová [a], Radoslav Sovják [b]

[a] Czech Technical University in Prague, Faculty of Civil Engineering, Department of Mechanics, Thákurova 7, 166 29 Prague 6, Czech Republic
[b] Czech Technical University in Prague, Faculty of Civil Engineering, Experimental Center, Thákurova 7, 166 29 Prague 6, Czech Republic

ARTICLE INFO

Keywords:
Microcracking (B)
Shrinkage (C)
Creep (C)
Concrete (E)
Modeling (E)

ABSTRACT

The material models for creep and shrinkage operating on the material point level in FEM are usually intended for challenging complex applications and structures, where the average cross-sectional approach does not suffice. The identification of the growing number of material parameters induced by increasing model capabilities relies on very specific and narrow-oriented yet interconnected experiments which are scarce. The presented comprehensive experiments aim to provide a clearer image of the complicated interaction among the basic phenomena: drying, shrinkage, creep, and microcracking. The cornerstone of this ongoing research is a unique set of 30 partially-sealed unreinforced concrete beams with span 1.75–3.0 m subjected to drying.

To minimize material variation, all specimens in this study were cast from a single batch of ordinary strength structural concrete with slag-blended binder. The resulting experimental database will be suitable both for validation and development of the constitutive models.

1. Introduction

The time-dependent behavior of concrete characterized chiefly by its creep and shrinkage is inherently associated with the serviceability and durability of all concrete structures. The ambient conditions affect both creep and shrinkage which are often tightly connected. Concrete drying gives rise to non-uniform shrinkage strain which produces tension even in members without external restraint and can cause cracking. At the same time these stresses are relieved by creep which is further accelerated by changes in relative humidity [1,2].

The sensitivity of particular structure to creep and shrinkage predetermines the method which should be employed in structural analysis. As stated in [3], a scale with 5 grades which span from concrete frames through medium-span bridges to super-tall buildings can be used for such classification. According to this scale, the models from the design codes and recommendations suffice for the analysis of the first three grades least sensitive to creep and shrinkage. These models which employ an average cross-sectional approach and are suitable even for hand-calculations were developed and calibrated based on a large number of experimental results collected in databases. Typically, the experiments in such databases have very similar setup but vary in material properties. The power of these models resides in the relationship among the composition and the overall creep and shrinkage response; therefore, the primary input parameters are the concrete composition and strength. In contrast to this, the material-point approach embedded in coupled FEM simulations is intended for challenging complex applications and structures where the simpler models do not suffice. The models can describe processes and phenomena which become wiped out by the averaging in the cross-sectional approach.

Even though the description of the underlying mechanisms of creep and shrinkage remains partially unknown even nowadays, the predominant origin of these processes is deemed to be at the micro- and nano-scale of cement paste. For this reason the governing equations of the advanced models contain a mixture of material parameters, some are of which related to the simplified physically-based processes on the lower scales, the other are phenomenological and arrive either from upscaling to the concrete level or simply from experimental observations.

These models often rely on supplementary tests necessary for their calibration and identification of their parameters. To compensate this effort, the models are capable of providing accurate predictions of the behavior under different conditions (size, loading, ambient conditions).

* Corresponding author.
E-mail addresses: petr.havlasek@fsv.cvut.cz (P. Havlásek), vit.smilauer@fsv.cvut.cz (V. Šmilauer), lenka.dohnalova@fsv.cvut.cz (L. Dohnalová), sovjak@fsv.cvut.cz (R. Sovják).

https://doi.org/10.1016/j.cemconres.2021.106402
Received 26 August 2020; Received in revised form 1 February 2021; Accepted 14 February 2021
Available online 10 March 2021

The scope and the setup of the majority of the experiments from the databases hinder calibration of the complex models. Moreover, the available experimental data are often insufficient for thorough validation of the newly developed models, such as the model based on poromechanics [4] by Aili [5] or the two recently proposed improvements of the Microprestress-Solidification theory [6,7].

For example the most comprehensive experimental database assembled at Northwestern University comprises over 900 distinct concrete mixes with more than 60,000 data points. Despite this extraordinary extent of data, only 19 experimental data sets examined drying shrinkage and both basic and drying creep on compatible specimens and setup which is necessary for proper calibration of the complex material models. From that only 9 studies fulfill the supplementary requirements such as completeness of the experimental description or sufficient duration of the experiment which is vital for relevant evaluation of the interaction between drying shrinkage and creep of ordinary structural concretes.

Furthermore, none of these references contains additional information of the moisture loss or the internal distribution of relative humidity which is deemed to be the driving force for shrinkage and drying creep. In general, the database contains very little entries containing blended cements with blast furnace slag which makes the current research beneficial also in this respect.

The aim of the project at CTU in Prague is to assemble a thorough experimental data set oriented on long-term behavior of concrete exposed to drying which can be used for validation of the presently used material models as well as for their future development. To minimize the variation and to provide a clearer image of the complicated interaction among the basic phenomena — drying, shrinkage, creep, and microcracking — all specimens are prepared from a single concrete batch and the concrete mixture is designed to yield a typical ordinary-strength structural concrete. The core of the current experimental investigation is represented by 30 partially-sealed unreinforced concrete beams subjected to drying and loading by self-weight, their spans range from 1.75 m to 3.0 m.

A recent experimental-numerical study on identification of intrinsic creep properties [8] examined the behavior of concrete beams loaded in four-point bending with either entirely sealed surface or with the top and bottom surfaces exposed to drying. In such setup the relative humidity becomes distributed symmetrically over the cross-section which, owing to the joint action of drying creep and microcracking, leads to increased compliance but does not produce shrinkage-induced curvature. In contrast to this, in the present experiment the majority of the beams are drying from one side only. The resulting non-symmetric distribution of relative humidity and shrinkage strains over the thickness gives rise to non-negligible curvature. This setup magnifies the monitored deflections which puts less demand on the accuracy of measuring techniques involved and also diminishes the microcracking as the structural restraint becomes smaller. These measurements are supplemented by more conventional creep, eccentric creep [9], shrinkage and strength experiments.

The experiment started one year ago and will last at least two more years. The present paper describes the experimental setup and summarizes the experimental results collected within the first year of the experiment. Whenever it is possible, the data are compared to the closed-form expressions presented in the design codes and recommendations, namely the B3/B4 models [3,10] and the *fib* Model Code 2010 [11] (further referred to as *fib*). The *fib* model was chosen because it offers a unified and compatible description for a wide range of physical properties of concrete and therefore it can be easily benchmarked against the data from the present experiment. Among numerous models for concrete creep and shrinkage, the B3 model was selected because it uses the same basic creep compliance function as the model based on the Microprestress-solidification (MPS) theory [12]. The modified MPS model [13,14] calibrated on very narrow data sets is used in the blind prediction of the long-term measurements and demonstrates the consistency of the measured data as well as suggests areas for its improvement.

2. Material and methodology

2.1. Concrete properties

All experimental specimens in this study were prepared from a single batch of ready-mix concrete with composition specified in Table 1. The chemical composition of the slag-blended cement is in Table 2, Blaine fineness 333 m^2/kg, hydration heat 266 J/g at 7 days according to prEN 196-11 with calorimetry data available from [15]. The relatively high water-to-cement ratio (from present perspective) w/c=0.49 was selected to guarantee sufficient workability without excessive admixtures and also to diminish the autogenous shrinkage.

As illustrated in Fig. 1 (obtained with ZEISS Axio ZOOM V16), both the coarse and fine aggregates were quarried from the river. The particles are mostly pebble-shaped with smooth surface. The details are summarized in Table 3.

The basic mechanical properties of concrete at the age of 27 days are summarized in Table 4. Compressive strength and Young's modulus were measured on cylinders ∅150 × 300 mm (EN 12390-13 [18], EN-12390-3 [19]). Even though the concrete mixture contained rapid-hardening cement 32.5 [20] the evolution of both compressive strength and stiffness is more accurately captured using *fib* formula with s=0.38 corresponding to cement 32.5 N (Fig. 2). This is due to the presence of slag which results into slower hydration kinetics but significant increase in strength even beyond the age of one month.

The properties in tension were determined using nonlinear FEM simulations of bending beams 100 × 100 × 400 mm with or without a notch. The notched specimens (25 mm and 40 mm notch depth, 3 specimens each) were tested in three-point bending while the remaining 4 unnotched beams were loaded in four-point bending. The simulations in OOFEM used isotropic damage model with exponential softening and crack-band regularization. The material parameters were determined by inverse analysis aiming at the best agreement with the experimentally measured load vs. displacement and load vs. notch opening relationships. This identification was done for each specimen and the resulting average values, summarized in Table 4 slightly exceeded *fib* prediction (f_t=2.82 MPa and G_f=140 N/m).

2.2. Experimental setup

The key part of the experimental plan outlined in Table 5 is devoted to behavior of slender beams subjected to the combination of symmetric and non-symmetric drying and bending. Those measurements are accompanied by more ordinary measurements and short-term tests which should facilitate identification of material parameters. The experiment started on April 13th 2019 when a single batch of ready-mix concrete was delivered and cast into prepared molds. All specimens were cast within 3 h from concrete delivery; afterwards, a simple tent covered with PE foil was put up above the specimens to protect them from excessive drying and two powerful fog generators helped maintaining high level of relative humidity (around 95%). The setting time was approximately 1.5 h after the end of casting. After several days the specimens were covered with PE foil and damp burlaps, and were regularly sprinkled with water. The small specimens (including the

Table 1
Concrete composition.

Ingredients	Quantity [kg/m^3]
Cement CEM II/B-S 32.5R, Radotín	379
Water	185
Aggregates (fine 822, coarse 969)	1791
Superplasticizer Sika BV4	1.9

Table 2
Chemical composition and characteristics of the blended cement CEM II/B-S 32.5R (GBFS content 29 wt%) as specified by the manufacturer.

Component	Wt%
CaO	57.2
SiO_2	24.6
Al_2O_3	5.6
Fe_2O_3	2.1
MgO	4.2
SO_3	2.1
K_2O	0.81
Na_2O	0.22
Insoluble residue	1.2
Loss on ignition	3.1

standard specimens for the mechanical properties, Table 4) were demolded at the age of 27 days and were moved to a closed container with relative humidity ≈95%. Larger specimens were kept in fiberboard molds under the PE foil until they became successively sealed (≈1 week). The following sections present the experimental setup in more detail.

2.2.1. Sealing quality and long-term functionality

In the experiment of Bryant [21] the specimens were sealed with one layer of 0.035 mm thick aluminum foil which corroded after 1 year and caused unintended moisture leakage. To prevent such behavior, the sealing in the present study combines metallic and plastic foils, namely 3 layers of self-adhesive aluminum foil thick 30 μm (Alufix by Korff) and 1 layer of 46 μm industrial grade polypropylene film packaging type with a synthetic rubber adhesive (3M 371). After demolding the surfaces were smoothed, vacuum-cleaned and the first layer of aluminum foil was applied to the surface followed by the plastic tape and finally two more layers of aluminum. The purpose of the first layer of aluminum was mainly to provide a smooth and adhesive surface for the plastic foil which does not stick to concrete.

In order to assess the functionality and quality of this improved design, several cubes 70 mm and 100 mm were wrapped with 1, 2 and 3 layers of aluminum foil and with the combined materials as described earlier and their weight was regularly measured.

2.2.2. Moisture loss

The amount of moisture lost due to drying was measured on concrete cylinders (Figs. 3, 10) which were cast into permanent molds made of PVC tube DN 200 SN 4 with (inner) ∅190.2 mm. The height of the cylinders was (on average) 28 mm, 51 mm, 102 mm, 150 mm, and 200 mm and the selected setup allowed to simplify the transport as one-dimensional. The entire perimeter of the PVC tube and narrow rims of the bases were sealed with the aluminum foil to prevent unintended moisture leak especially from the gap between concrete and PVC which might open due to shrinkage. Drying was possible from both surfaces and so the effective thickness was equal to the cylinder height. The moisture loss of the cylinders and of the sealed cubes (Section 2.2.1) was regularly monitored using laboratory balance Kern & Sohn GmbH 572–55 with weighing capacity 20 kg and precision 0.05 g.

2.2.3. Short-term creep

Stressing the prismatic specimens in the long-term creep test (Section 2.2.4) was a gradual process which took, according to the target load level, from 6 to 12 min. At such slow loading rate (≈0.83 MPa/min) it is impossible to assess the often discussed relationship between the conventional static modulus and the compliance function. For this

Table 3
Classification of aggregates.

Size and origin	Quantity [kg/m^3]	Petrology [approx. % vol.], [16,17]
0–4 mm, Nučničky	603	Quartz (50), biotite granitoids (20), sedimentary rocks (20), metapelite (10)
0–4 mm, Otradovice	219	Quartz (70), sediments (16), quartzite, mica schists, gneiss (8), biotite granites (3), feldspar (3)
4–8 mm, Ledčice	331	Quartz (65), sediments (20), phyllite, metabasite (5), plutonic rocks (6), feldspar (4)
8–16 mm, Nučničky	638	Quartz (50), biotite granitoids (20), sedimentary rocks (20), metapelite (10)

Table 4
Concrete mechanical properties at the age of 27 days.

Property	Unit	Value
Compressive strength, f_c	[MPa]	36.8 ± 1.4
Young's modulus, E	[GPa]	30.3 ± 0.3
Tensile strength, f_t	[MPa]	3.38 ± 0.45
Fracture energy, G_f	[N/m]	150 ± 21

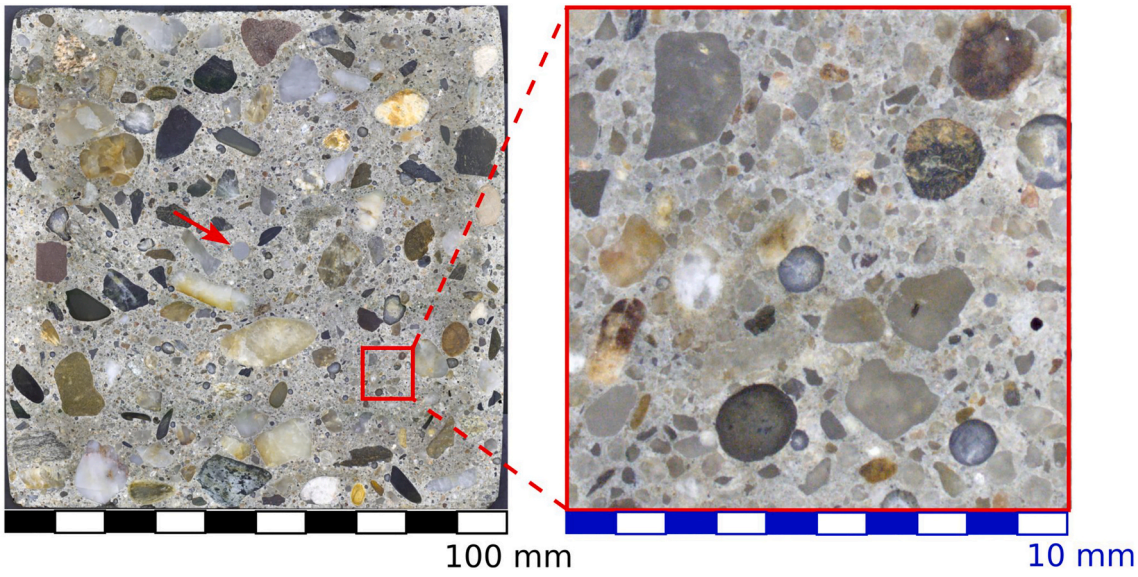

Fig. 1. Image of concrete microstructure in redundant beam with 100 × 100 mm cross-section. Image orientation corresponds to the casting position. The arrow indicates the position of 4 mm threaded bar.

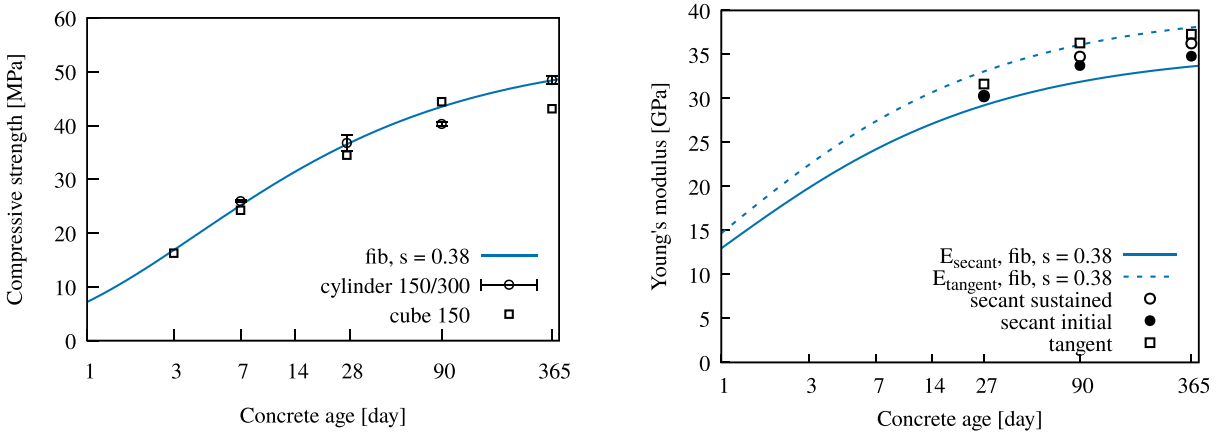

Fig. 2. Evolution of cylinder compressive strength and Young's modulus of concrete and the prediction with *fib*. Strength on cubes was multiplied by 0.85 to yield cylinder strength.

Table 5
Experimental specimens for long-term measurements, onset of drying, t_0, is measured from concrete set (5 h after mixing).

Objective	Geometry	Dimensions [mm]	t_0 [day]
Moisture loss	Cylinder	∅200 × 28 – ∅ 200 × 200	27.9
Shrinkage	Prism	100 × 100 × 300	28.3
Creep	Prism	100 × 100 × 300	28.0
Drying shrinkage, creep, microcracking in bending	Beam	from 100 × 50 × 1950 to 100 × 200 × 3200	34.1
+ loading/unloading	Beam	100 × 100 × 2200	33.3

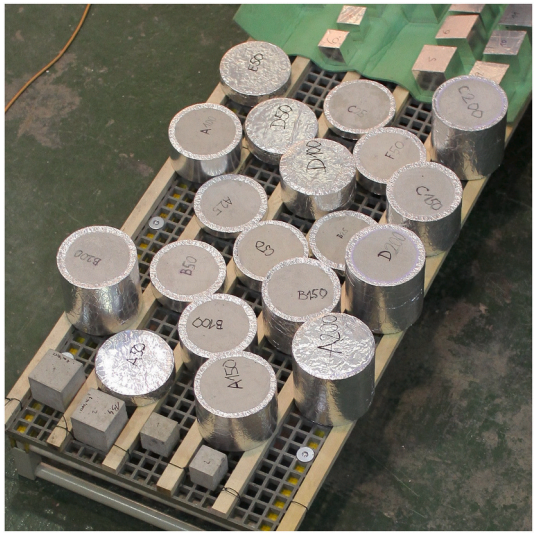

Fig. 3. Partially sealed concrete cylinders for moisture loss measurement and entirely sealed specimens for additional verification of the sealing setup.

reason the long-term creep measurements were supplemented by 1 h long short-term creep test in which the specimen is stressed by hydraulic testing machine in 30 s to one third of its expected strength. Such tests were conducted at the age of 27 days and 3 months at loading rates 0.38 MPa/s and 0.48 MPa/s, respectively, on standard concrete cylinders ∅150 × 300 mm. The evolution of axial strain was measured using a pair of 150 mm long extensometers placed on the opposite sides of the specimen.

2.2.4. *Shrinkage and creep on prisms*

Shrinkage and creep in sealed and drying conditions were measured on prismatic specimens with a square cross-section 100 × 100 mm and length of 300 mm. The longitudinal strain was on each specimen recorded with a pair of 150 mm long vibrating wire strain gauges (VWSG, Sisgeo 0VK4000VS00) installed at mid-height on the opposite surfaces (Fig. 5). Their mounting blocks were welded to L-shaped steel profiles 25 × 25 mm (Fig. 4). At the age of 28 days the specimens for creep were loaded and the companion shrinkage specimens were exposed to drying.

Axially loaded creep specimens were loaded by 100 kN force resulting into 10 MPa compression. Axial loading was guaranteed by steel bearings placed at both ends of each specimen (Fig. 6). After subtracting the deformation of the companion sealed or drying specimens and subsequent dividing by the imposed stress, the measurements delivered basic creep compliance (entirely sealed prisms, 2 specimens) or total creep compliance (two opposite vertical surfaces exposed to drying, 1 specimen), respectively.

The loading force was reduced to 50 kN in the case of eccentric compression (two opposite vertical surfaces exposed to drying, 2 specimens). The intention was to produce (initially) linear distribution of vertical stress over the cross-section with 10 MPa compression on one drying surface and 0 MPa on the other. The position of the force leading to such distribution coincides with one vertex of the central core and so the resulting eccentricity is 100 mm/6=16.7 mm.

Fig. 4. Steel mold equipped with sacrificed L-shaped profiles for creep and shrinkage prismatic specimens.

Fig. 5. Companion prismatic specimens with externally mounted VWSG for total (left) and autogenous (right) shrinkage assessment.

Fig. 6. Creep rig during loading.

2.2.5. Non-symmetrically drying beams

The core part of the experimental survey is a long-term monitoring of vertical deflection of concrete beams with several alternatives of the sealing setup. The thickness of all specimens is 0.1 m and in all cases the lateral sides are sealed. There are two major groups of specimens. The beams in the first set (Group I, 7 × 3=21 specimens, Fig. 7) have various span, height and are subjected to constant loading produced mainly by their self-weight. The specimens in the second set (Group II, 3 × 3 =9 specimens, Fig. 8) examine the influence of microcracking on unloading and reloading.

The geometry of the specimens in Group I (Table 6, Fig. 7) was designed to produce similar magnitude of the (initial) compressive and tensile normal stress due to bending (σ_x=1.035–1.078 MPa) and quasi-elastic deflection (0.34–0.47 mm). Three identical specimens were prepared of each configuration to assess the material variability.

The development of deflection produced by drying shrinkage differs among the specimens owing to their different height as well as due to the sealing setup. A quantity usually called *effective thickness* defined as $D=2V/S$ where V and S are the volume and surface exposed to drying, respectively, is typically the most significant factor which determines the kinetics of the drying process in the design codes. Here, D ranges from 100 mm to 400 mm. With the exception of the largest specimens (#6, 200 mm height, 2 × 30 kg weight 0.6 m from the support) the loading is only due to self-weight of the concrete beams.

All specimens from Group II (Fig. 8) had 2.0 m span, total length 2.2 m, and height 0.1 m. There are three configurations of the sealing setup—drying upwards, drying downwards and entirely sealed—each represented by 3 specimens. The loading history could be modified by a pair of 15-kg external weights placed 0.4 m (L/5) from the support. One specimen in each sealing configuration was loaded by the external weights continuously from the beginning, i.e. from the age of 33.3 days. The loading history of the second and third specimen was more complex in order to assess the influence of aging and microcracking on the loading and unloading stiffness and short-term creep. In particular, the external 15-kg weights were moved from the second to the third specimen (in each configuration) one month after the first loading and then returned back one year after the first loading.

Fig. 7. Set of 7 × 3 beams (Group I) with permanent loading, minimum span 1.75 m and maximum span 3.0 m.

For safety reasons the beams were reinforced with a single longitudinal rebar ∅4 mm which was placed in the center of the cross-section (Fig. 1) to minimize its influence on the investigated behavior. The casting position was perpendicular to the destined terminal orientation and so the height of all molds was identical, 100 mm.

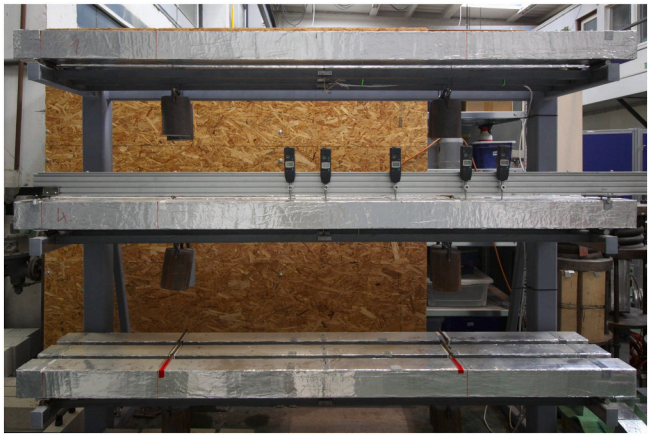

Fig. 8. Set of 3 × 3 beams with 2 m span (Group II) and illustration of deflection reading at specific locations using 5 digital indicators.

Approximately 1.5 month after casting the redundant specimens were cut into ≈0.5 m long pieces and weighed to determine the actual concrete density which causes the dominant loading in addition to drying shrinkage. The average density was 2309.8 ± 10.9 kg/m^3. After additional two months the density dropped to 2290 kg/m^3. In the computations the density is treated as constant 2300 kg/m^3.

The vertical deflections of the beams are monitored using different experimental techniques. The results presented here were obtained with a set of 5 digital indicators (Mitutoyo 575-121 with range 25.4 mm and accuracy 0.02 mm) mounted at fixed positions to an aluminum extrusion profile (Fig. 8). Four positions of the gauges correspond to the midspan of the beams (0.875 m, 1 m, 1.25 m, 1.5 m from the left support), while the last gauge is placed at 1.625 m to mirror the first gauge on the most frequent beams with 2.5-m span and to assess whether the deflection line remains symmetric over time. In the case of Group I, this measuring technique was implemented only on the beams placed in the front position, the geometrically identical specimens (middle and back position of each shelf) were measured only using the digital image correlation (DIC, results unavailable at the time of writing and will be published in a separate paper). The vertical and horizontal displacements related to the

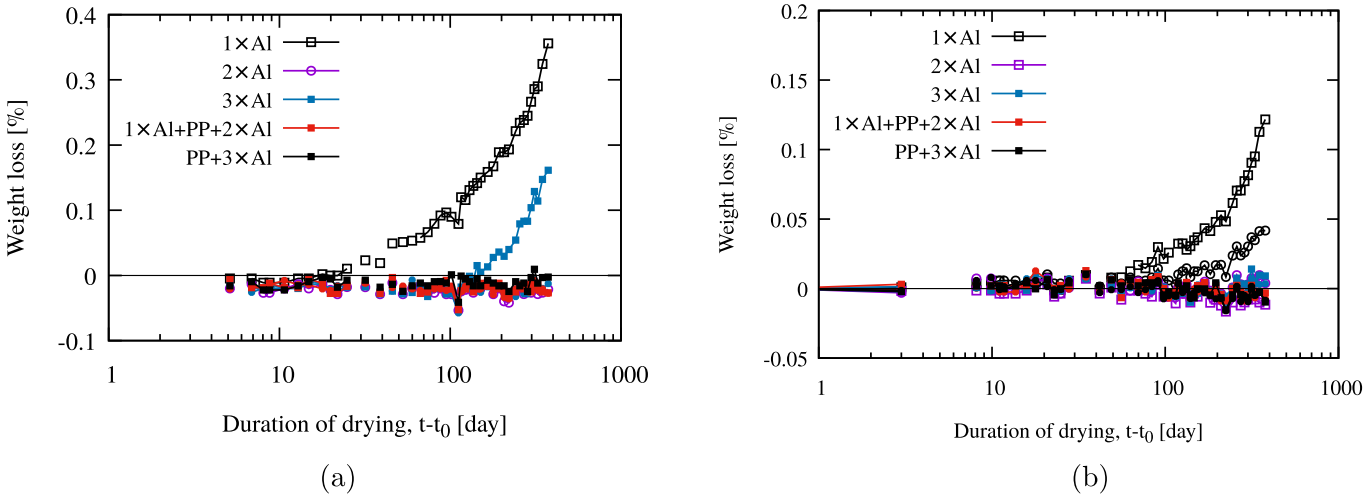

Fig. 9. Moisture loss (with respect to initial weight) measured on 70 mm (a) and 100 mm (b) cubes. Legend describes the sealing setup (ordering from the interior outwards), Al = aluminum and PP = polypropylene foil.

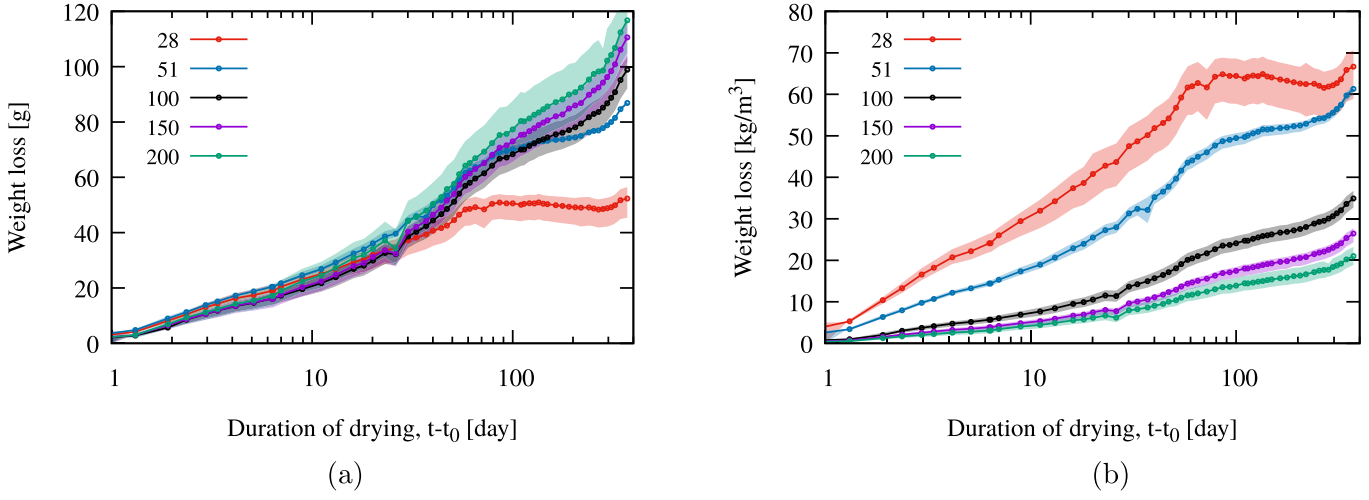

Fig. 10. Moisture loss measured on concrete cylinders with different heights (a) and normalized per concrete volume (b).

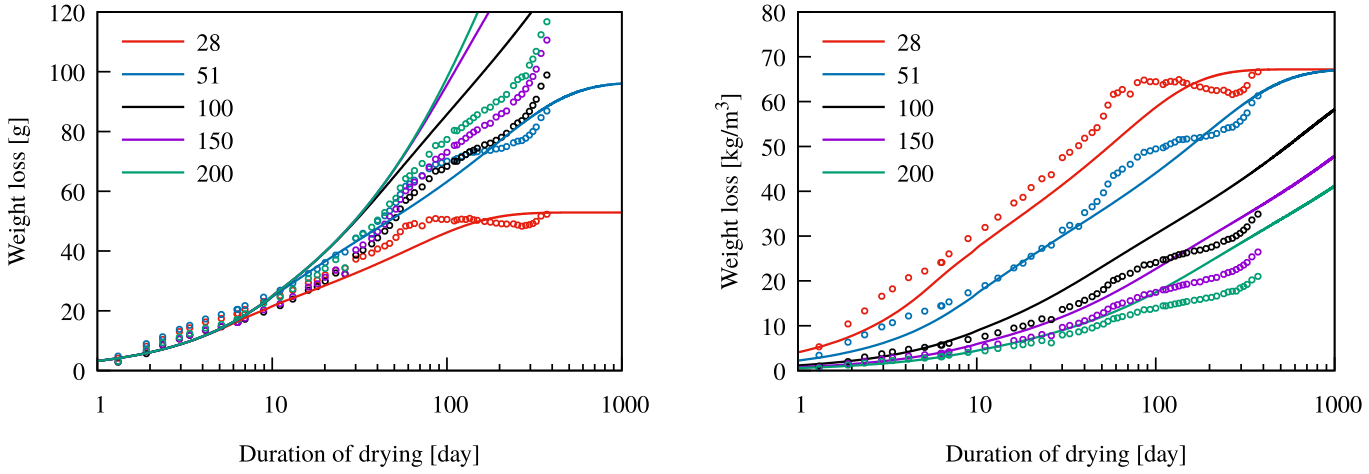

Fig. 11. Measured (points) and predicted (smooth lines) moisture loss of concrete cylinders with different heights.

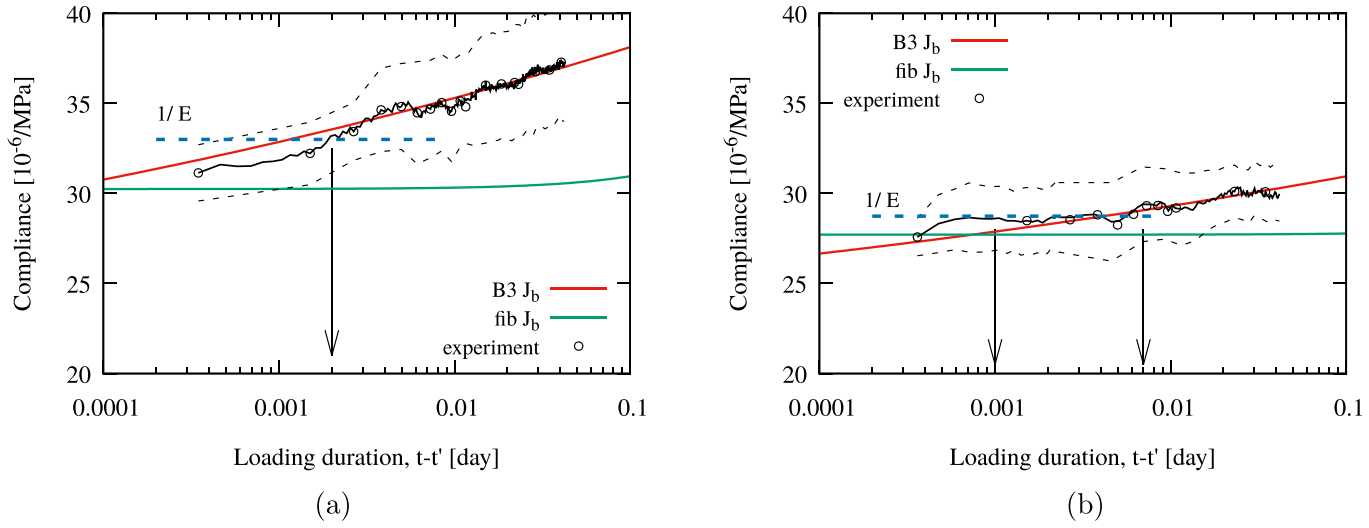

Fig. 12. Short-term compliance from 1-hour creep tests at the age of 27 days (a) and 3 months (b). Blue lines denote reciprocal Young's modulus determined in a separate experiment at respective age. (For interpretation of the references to color in this figure legend, the reader is referred to the web version of this article.)

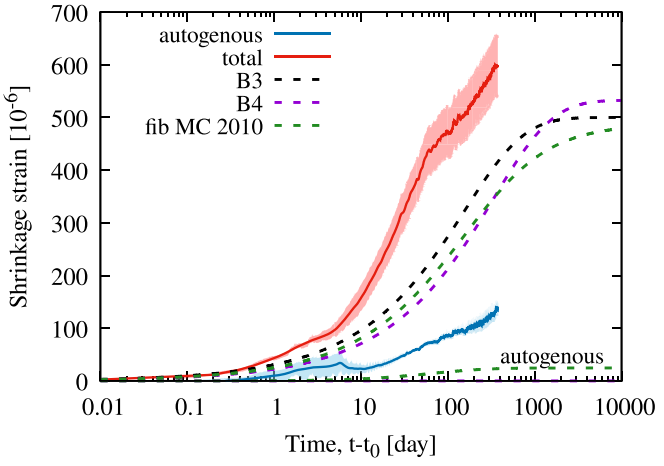

Fig. 13. Evolution of autogenous and total shrinkage and the blind prediction with cross-sectional models. Note that the autogenous shrinkage strain does not contain the response prior to 28 days.

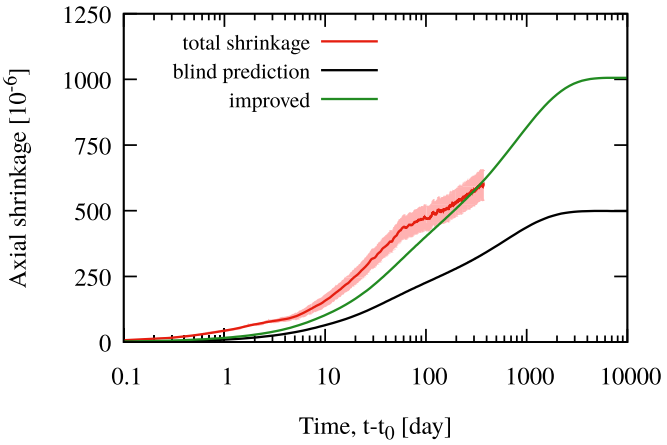

Fig. 14. Experimentally measured total shrinkage vs. blind (ultimate shrinkage 500 $\mu\varepsilon$) and updated (1000 $\mu\varepsilon$) prediction using FEM.

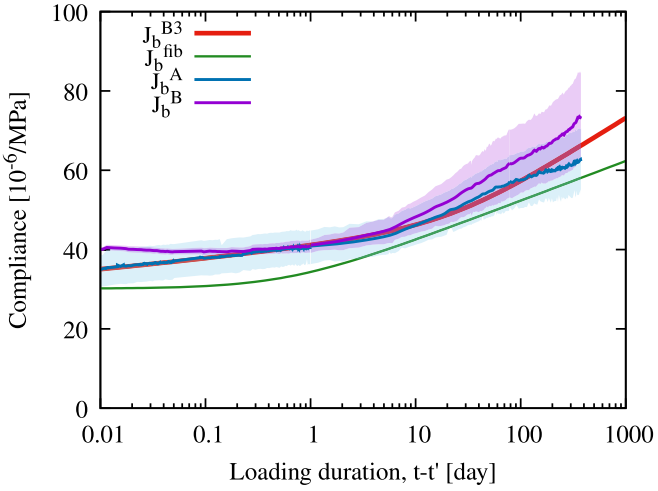

Fig. 15. Comparison of the predicted and measured basic creep, measurements adjusted to match the short-term compliance. Solid curves represent the average of the readings which are the boundaries of the shaded areas.

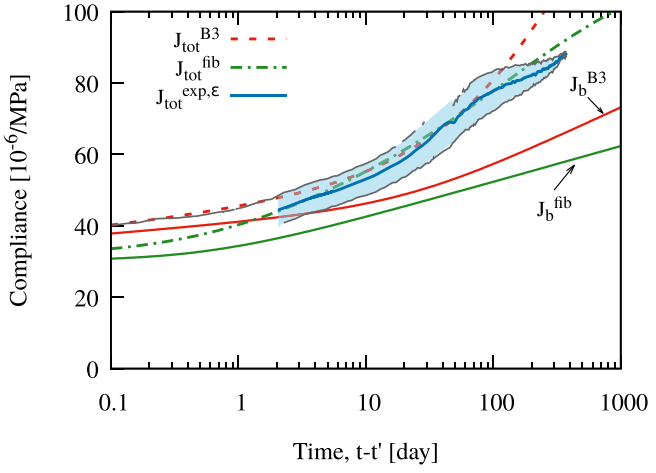

Fig. 16. Comparison of predicted and measured axial total creep. Solid curves represent the average of the readings which are the boundaries of the shaded areas.

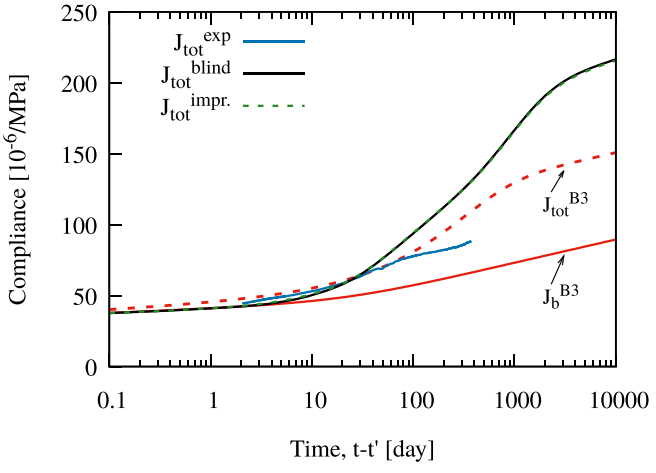

Fig. 17. Comparison of predicted and computed axial total creep using FEM.

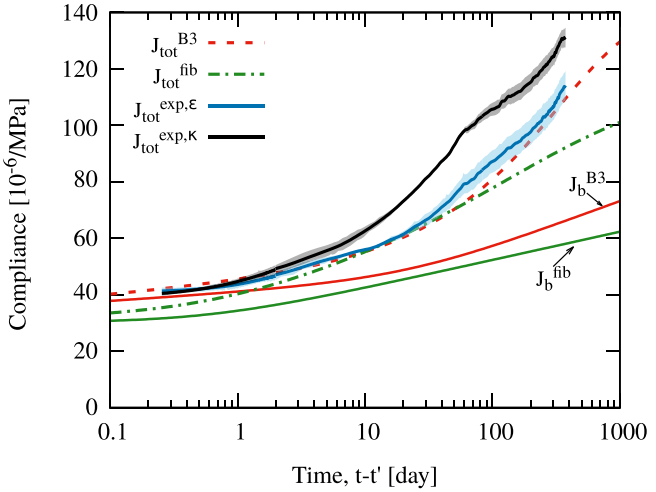

Fig. 18. Comparison of the predicted and measured total compliance (shortening and bending separately) under eccentric compression. Measurements compensated for drying shrinkage and adjusted to match short-term compliance.

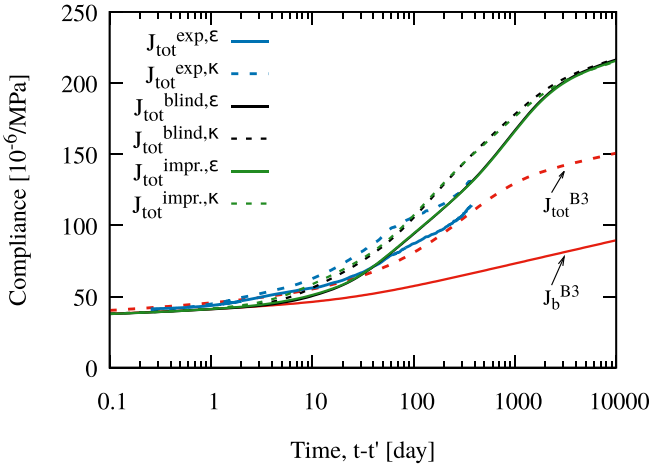

Fig. 19. Comparison of the experimental data and FEM simulation under eccentric compression.

reference measurements above the supports will be available at the midspan and quarter-spans of each beam and will provide evidence of the variation among specimens.

Each beam in Group II is equipped with a potentiometric linear transducer with internal spring return (MMR10-12, effective stroke 12.7 mm, total resistance 10 kΩ) mounted underneath at the midspan.

2.2.6. *Ambient conditions*

The experiment is located at the large laboratory hall of the Faculty of Civil Engineering, CTU in Prague. The ambient conditions are subject to annual but also daily fluctuations (lower temperature dropping to 15 °C during weekends in winter). On average the relative humidity was ≈50% during the first year; temperature was ≈20 °C in autumn and spring, 25 °C in summer, and 17 °C in winter.

2.3. *Material models and modeling*

The finite element simulations in this study demonstrate not only the capabilities of the advanced constitutive models for concrete, but also indicate the consistency of the measured data. All coupled finite element simulations were run in a staggered approach with the humidity transport preceding the mechanical analysis (one-way coupling only).

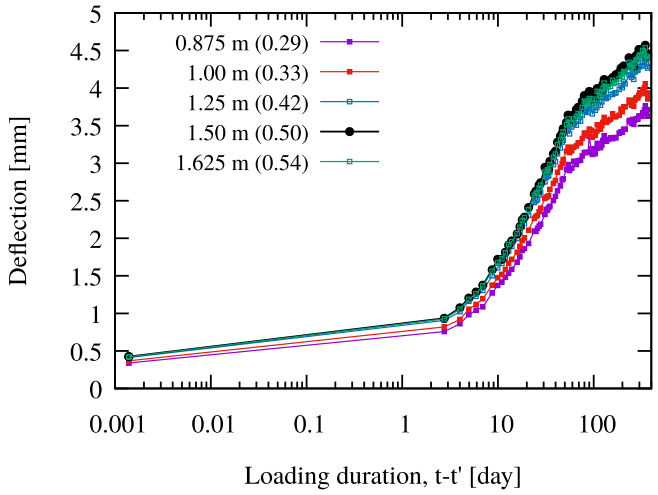

Fig. 20. Development of vertical deflection measured at specific locations on a beam with 3 m span and 150 mm height by digital dial gauges. Legend describes the position from the left support and its normalized value by the span is in parentheses.

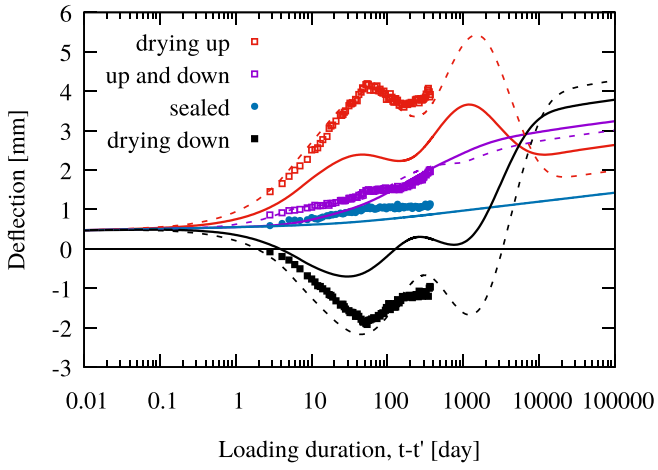

Fig. 21. Vertical deflection of beams #1–#4 from Group I with 2.5 m span and 100 mm height compared against FEM prediction. Solid lines = blind prediction, dashed lines = improved prediction.

The Bažant and Najjar [22] model for diffusion of water vapor is used to solve the moisture transport. The dependence of diffusivity on relative humidity, h, is highly non-linear and can be approximated as

$$D(h) = D_1\left(\alpha + \frac{1-\alpha}{1+\left(\frac{1-h}{1-h_c}\right)^n}\right) \quad (1)$$

The *fib* recommends the parameters as α=0.05, h_c=0.8, n=15, and based on the compressive strength D_1=30.5 mm^2/day. The initial value of relative humidity was set to 0.98 which is a typical value for concrete at sealed conditions [1] and quite high value w/c=0.49 allows to neglect the sink term. The mixed boundary condition is assigned to the drying surface. The condition reads $J_h = f \cdot (h_{\text{env}} - h)$ where J_h is the humidity flux and f is the surface factor set to 1 mm/day [14,23].

The constitutive model for structural analysis combines a linear viscoelastic material model based on a modified MPS theory with a softening smeared cracking model in tension. The models are linked in series such that the total deformation is obtained as a sum of the two contributions while the stresses are the same. The model is formulated incrementally. The new stress vector in time step $i+1$ is computed from

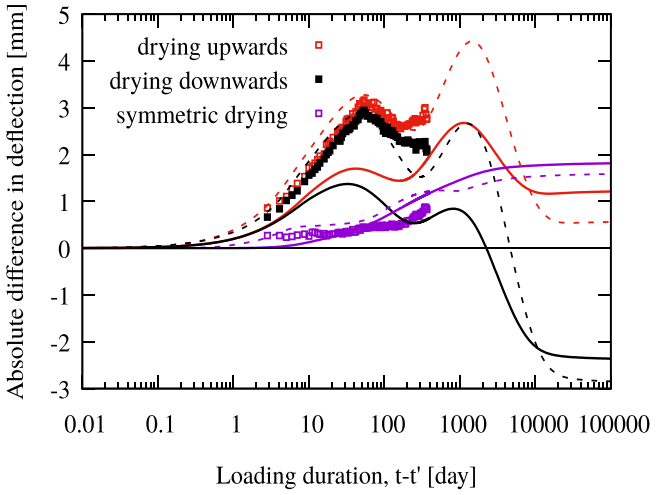

Fig. 22. Absolute value of deflection caused only by nonuniform drying (combined effect of shrinkage, microcracking, drying creep) measured on beams with 2.5 m span and 100 mm height (#1–#4 from Group I). Solid lines = blind prediction, dashed lines = improved prediction.

the preceding equilibrated stress vector σ_i and the product of the viscoelastic stiffness matrix $\overline{\mathbf{D}}_{ve}$ and the increment of the reduced strain vector

$$\sigma_{i+1} = \sigma_i + \overline{\mathbf{D}}_{ve}(\Delta\varepsilon - \Delta\varepsilon'' - \Delta\varepsilon_{sh} - \Delta\varepsilon_T - \Delta\varepsilon_{cr}) \quad (2)$$

where $\Delta\varepsilon$ is the total strain increment, $\Delta\varepsilon''$ strain increment due to creep, $\Delta\varepsilon_{sh}$ is the shrinkage strain increment, $\Delta\varepsilon_T$ is the thermal dilation increment, and $\Delta\varepsilon_{cr}$ is the cracking strain increment.

The rheological behavior is described using the model derived from the Microprestress-solidification (MPS) theory [12] which was modified to eliminate the opposite size-effect on drying creep [13,14]. Under hygrally sealed conditions and constant room temperature the model reduces to the basic creep compliance function of the B3 model which is entirely described by four parameters only, q_1–q_4. Based on concrete composition and 1-month compressive strength, their values can be estimated using prediction formulae whose applicability is limited to Portland cement concretes only [3]. Despite this restriction, the following values of q_1–q_4 were determined using total cement content (including slag): 20.9, 140.8, 2.32, 6.85, all in 10^{-6} MPa^{-1}.

In concrete, drying leads both to stress-dependent and stress-independent deformation. The evolution of the additional compliance due to drying can be described according to the MPS theory by a differential equation for the microprestress. Any changes in relative humidity lead to its generation while at constant condition it relaxes. In the current setup this governing equation is linear. Microprestress is directly related to the compliance of an aging dashpot, the deformation is thus treated as irreversible upon unloading. Dimensionless parameter k_3 has the strongest influence on drying creep. In the previous analyses its optimum value varied between 1 [24] and 90 [14]. The drying creep of CFRP pre-stressed beams loaded in bending was best captured with k_3=30 and 35 [23], and a very similar value yielded good agreement with the experiment of Bryant and Vadhanavikkit [14]. The present simulations assumed k_3=30 by default. Surprisingly similar value (k_3=30–40) works well also for the drying creep of hardened cement paste [25]. The viscoelastic behavior under variable humidity also depends on three parameters α_E, α_R, α_S which determine the evolution of transformed times based on the history of relative humidity at given material point. The parameters are set to their default values, α_E=10, α_R=0.1, α_S=0.1.

As shown in [23] the concrete compliance dramatically increases when the prescribed history of the ambient relative humidity is not

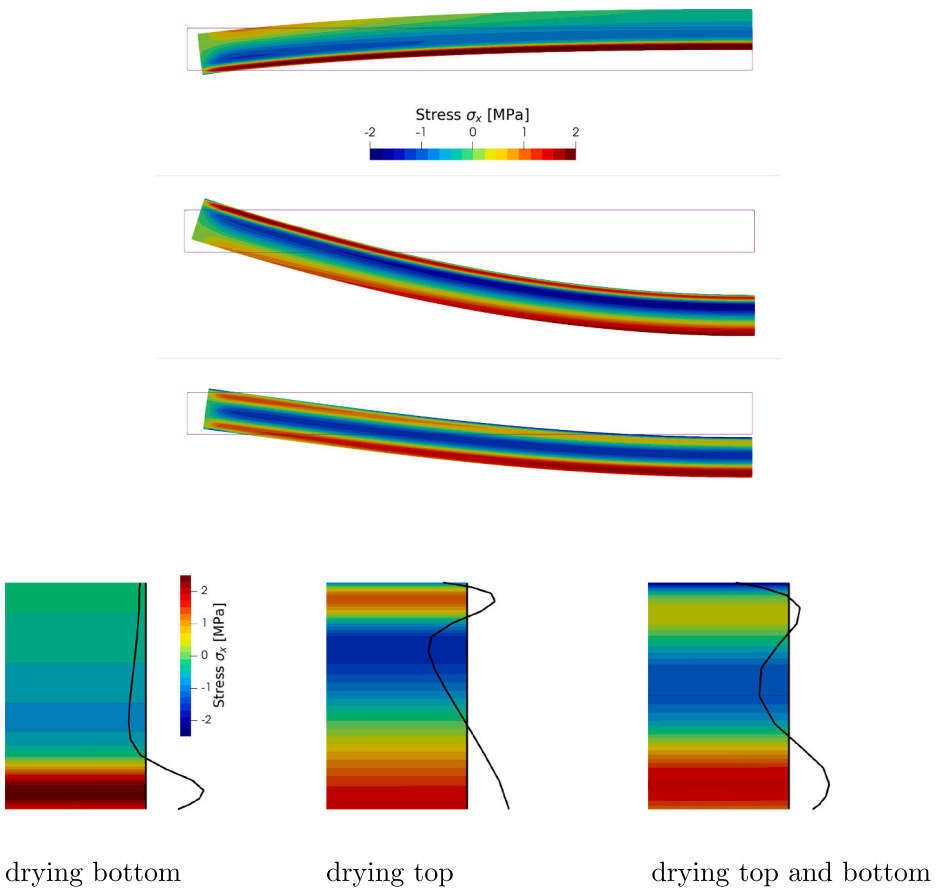

Fig. 23. Computed distribution of σ_x in beams with 2.5 m span drying from the bottom, top, and both top and bottom surfaces after 1 year (ordering from the top). The deformed shape is 50× magnified. The slices are drawn at the midspan of the beams.

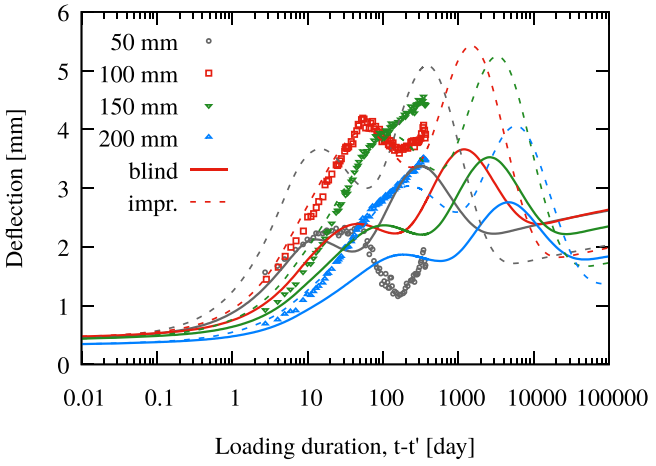

Fig. 24. Development of vertical deflection at the midspan of beams drying from the top surface and with different heights.

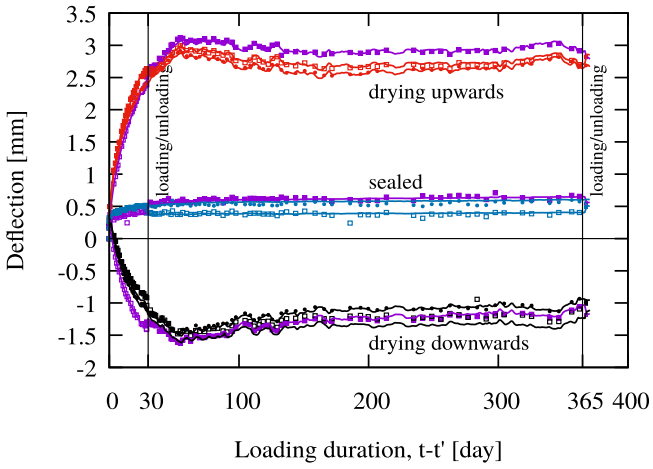

Fig. 25. Development of vertical deflection at the midspan of beams from Group II with 2 m span.

constant or monotonous. The compliance spuriously grows with the complexity of h_{env} whose oscillations generate more microprestress. To avoid these problems, ambient relative humidity is treated as a constant and set to h_{env} =0.5, and for similar reasons also temperature is set to the room temperature (T=20 °C) despite the model is temperature sensitive.

According to the MPS model, the rates of drying shrinkage and relative humidity are interlinked through

$$\dot{\varepsilon}_{sh} = k_{sh}\dot{h} \tag{3}$$

where k_{sh} is a shrinkage parameter. In the original model this parameter was a humidity and age-independent constant. In the "blind" prediction the constant was calibrated as k_{sh}=1.1 × 10^{-3} to yield the ultimate drying shrinkage strain 500 $\mu\varepsilon$ which is approximately the average value predicted with the cross-sectional models B3, B4 and *fib* as shown later in Fig. 13. Owing to the high water-to-cement ratio (w/c=0.49), the autogenous shrinkage is neglected in the prediction.

In the smeared cracking model which enhances the viscoelastic model, the crack orientation is defined by the direction of the principal

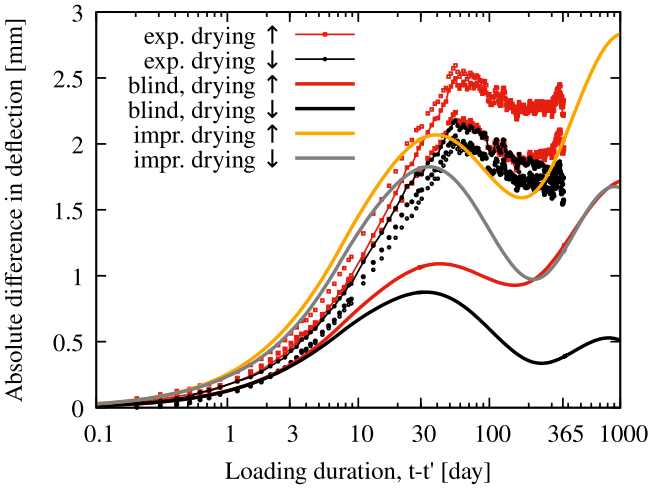

Fig. 26. Absolute value of additional deflection due to non-symmetric drying (combined action of shrinkage, microcracking, drying creep), comparison of measurement on beams from Group II and FEM predictions.

stress which attains the tensile strength. The tensile cracks can form in mutually perpendicular directions and after their initiation their orientation remains fixed [26]. Model objectivity is achieved using the crack-band approach [27]. This approach relates the cracking strain perpendicular to the crack plane with the crack width used in the traction-separation law of an exponential type. The characteristic length necessary to establish this conversion is considered as the finite element size projected in the normal direction to the crack plane. By fitting the experimental results of the bending experiments, the parameters of the softening law were identified as f_t=3.4 MPa and G_f=140 N/m (Table 4).

3. Results and discussion

In this Section, the data measured within the first year of the experiment are compared not only to the blind prediction of B3, B4 and *fib* models, but also to the results obtained from the coupled finite element simulations in the open-source FE package OOFEM [28,29]. In most of the cases, the highly non-uniform or non-symmetric stress field originating from the drying shrinkage does not allow to employ the average cross-sectional approach which makes the material-point approach the only option.

Even though the almost complete set of experimental data was available to the authors at the time when the finite element simulations were done, the problem was approached as if they were not. The intention was to demonstrate the prediction capabilities of the constitutive model but more importantly to reveal its limitations.

In the following text, t is used for time, t_0 for the onset of drying (is different for individual specimens as indicated in Table 5), and t' is the age at loading. Therefore, $t - t_0$ represents the duration of drying and $t - t'$ stands for the loading duration.

3.1. Sealing quality and long-term stability

Comparison of different alternatives of sealing in Fig. 9 demonstrates that one layer of aluminum is insufficient as all relevant specimens started losing weight already after one month. Additionally, probably due to improper handling during regular measurements, one specimen with three layers of aluminum started leaking after approx. 100 days. In the worst case the moisture loss related to the initial weight reached 0.35% which is around 10% of the loss measured on the unsealed companion specimens. The selected sealing setup which combines one layer of plastic and three layers of aluminum tape does not show any moisture leak in the first year of the experiment. This indicates that the present experimental study yields excellent results free from spurious drying.

3.2. Moisture loss

The experimentally measured moisture loss is presented in Fig. 10 in which the shaded region denotes the range between the minimum and maximum and the lines correspond to the average. Fig. 10a documents that in the first month of drying the moisture loss is almost identical independently of the thickness. A separation from the overall trend indicates the time when the opposite drying fronts met. This occurred after ≈1 and 3 months in the case of 28 mm and 51 mm thick specimens, respectively.

The moisture loss divided by the concrete volume in Fig. 10b allows to compare the extent to which the specimens with the same effective thickness have already dried. On contrary to the other specimens with higher thickness, the thinnest cylinders (28 mm) can be treated to have reached the equilibrium with the ambient conditions in the first year of the experiment. The moisture loss is ≈65 kg/m^3. The 100 mm and 200 mm thick cylinders have lost ≈50% and 30% of that value, respectively, which means that the corresponding partially sealed beams are still in the first half of the drying process.

Fig. 11 demonstrates that the simulations with the Bažant-Najjar model (parameters predicted according to *fib*) exhibit exceptional agreement with the experimental. The selected material model determines only the evolution of drying (distribution of relative humidity in time), not the moisture loss per se. The moisture loss can be easily obtained by integrating the decrease in moisture content over the volume; the moisture content can be evaluated from the computed relative humidity using the desorption isotherm. In the present case the moisture capacity (derivative of desorption isotherm) which gave the best match with the thinnest specimens (28 mm and 51 mm) was k=140 kg/m^3. Yet with such calibration the model tends to overestimate the moisture loss of the thicker specimens. This might be due to the combined action of the following factors:

- Concrete in the cylinders is not completely homogeneous over the thickness, the region closer to the surface contains more cement paste and thus more evaporable water while the coarse aggregates are in the center. Additionally, as a result of 16 mm aggregates in the concrete mixture, the thinnest specimens (28 mm and 51 mm thickness) might not be perfectly representative of the entire experimental set as they might contain higher amount of cement paste and thus more evaporable water.
- Concrete curing led to nonuniform moisture distribution over the thickness, on average thicker members contain less evaporable water.
- Thicker specimens contain enough moisture in the core for maintaining hydration. More water becomes chemically bound, reducing content of evaporable water.

3.3. Short-term creep

The B3 model shows an excellent agreement with the experimental data at both ages, see Fig. 12. At the age of 1 month (27 days), the experimental compliance function matches the reciprocal value of the conventional secant Young's modulus (horizontal blue lines) at $t - t' \approx 0.002$ days (2.9 min) as indicated by the arrow. At the age of 3 months, owing to reduced creep rate, the compliance is very close to $1/E$ on a longer interval, from 0.001 to 0.007 day (1.4 to 10 min). Green curves in Fig. 12 illustrate the prediction with *fib*. The material parameters comply with the preceding Sections. Interestingly, the short-term creep rate of this model strongly underestimates the measured data. Note that the instantaneous compliance of the *fib* model corresponds to the inverse of the initial (tangent) modulus which explains the apparent difference from $1/E$ which is the inverse of the conventional

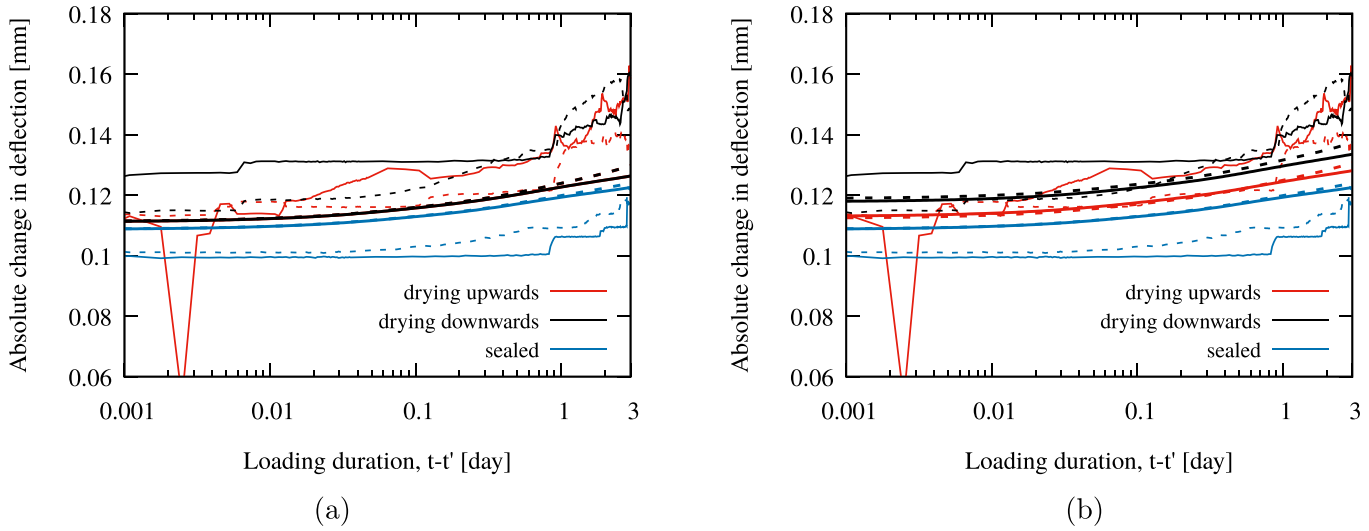

Fig. 27. Group II: absolute value of the short-term change in deflection caused by loading/unloading 1 month after the initial loading, blind prediction (a), improved prediction (b). Solid lines = loading, dashed lines = unloading, thick lines = FEM simulation, thin lines = experiment.

secant modulus. As was shown in Fig. 2, the *fib* model captures the evolution of the stiffness perfectly.

3.4. Shrinkage and creep on prisms

3.4.1. Autogenous and total shrinkage

The measured evolution of autogenous and total shrinkage and the prediction using B3, B4 and *fib* models are compared in Fig. 13. The shaded area indicates the differences of the measurement on the opposite surfaces (of the same specimen) while the solid line is the average. Initially very large scatter of autogenous shrinkage became negligible after 10 days of measuring. On the beginning of drying, the readings of total shrinkage were very uniform but after approx. two months of drying the scatter increased to ≈20%.

In the end of the first year, the measured total shrinkage reached 600 $\mu\varepsilon$ and autogenous shrinkage 150 $\mu\varepsilon$ (in addition to autogenous shrinkage ≈50 $\mu\varepsilon$ which occurred during curing period - prior to the age of 28 days when the measurement on prisms has started). In concrete with high water-to-cement ratio the autogenous shrinkage is typically negligible and so its magnitude might seem exaggerated. Yet as confirmed in other experiments, the autogenous [30–32] and drying [2,33,34] shrinkage increase with slag content and autogenous shrinkage can become substantial even at higher *w/c* [30]. These trends are not consistent in the literature (e.g. opposite tendency in [35]) but are prevailing.

The different cross-sectional models predict the total shrinkage very consistently not only in terms of its ultimate value but also the time evolution. However, both the autogenous and total shrinkage are underestimated. From the selected models only the *fib* gives nonzero autogenous shrinkage which is negligible compared to the measurement. The following setup of the prediction models was used. B3 model: α_1=0.85 (type II, modified cement), α_2=1.0 (curing in water or 100% relative humidity), B4 model: parameters for slowly hardening cement (SL) and limestone aggregates, *fib*: parameters for CEM 32.5 N.

As shown in Fig. 14 in the FEM simulations the shrinkage constant k_{sh}=1.1 × 10^{-3} had to be doubled to k_{sh}=2.2 × 10^{-3} to match the

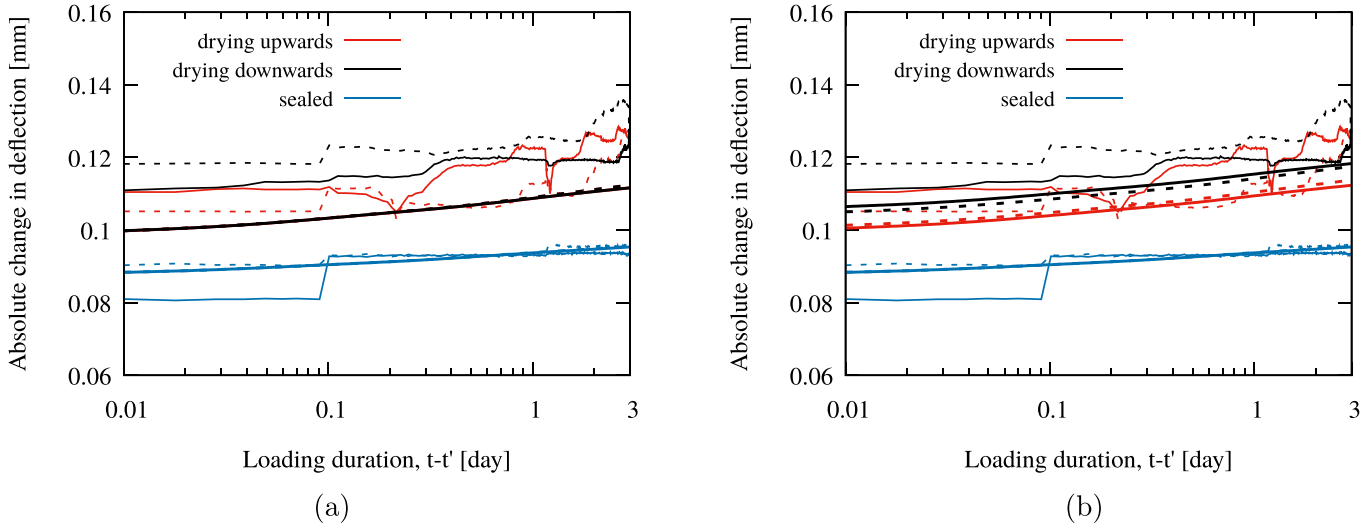

Fig. 28. Group II: absolute value of the short-term change in deflection caused by loading/unloading 1 year after the initial loading, blind prediction (a), improved prediction (b). Solid lines = loading, dashed lines = unloading, thick lines = FEM simulation, thin lines = experiment.

Table 6
Setup of the drying beams with permanent loading (Group I).

Row	Height [mm]	Span [mm]	Length [mm]	Drying	D [mm]
1	100	2500	2700	Top	200
2	100	2500	2700	Sealed	∞
3	100	2500	2700	Bottom	200
4	100	2500	2700	Top + bottom	100
5	50	1750	1950	Top	100
6	200	3000	3200	Top	400
7	150	3000	3200	Top	300

experimental data. In the following Figures the corresponding data series are labelled as "blind" and "improved", respectively.

3.4.2. Basic creep

The measured instantaneous deformation on prisms (not shown) was significantly higher than what was determined on concrete cylinders at the same age. The reason probably stems from the embedded L-shaped steel profiles which introduce heterogeneity in concrete. In Section 3.3 it was shown that the short-term creep was perfectly captured with the B3 model. Therefore, the experimental data were vertically shifted to match the B3 compliance for the duration of loading $t - t'$ from 0.2 to 1 day where the creep rate agrees with the model very well. The results compensated for the autogenous shrinkage strain are for the two specimens shown in blue and purple color in Fig. 15.

The prediction of the B3 model shown in red color gives slightly higher long-term creep rate than the *fib* (thinner green line) which also predicts lower initial compliance. (The initial compliance of *fib* model is strongly dependent on the aggregate type. More realistic instantaneous deformation could be obtained if the default "quartzite aggregates" (α_E=1) are replaced with "limestone" (α_E=0.9). However, quartzite aggregates gave good agreement with the Young modulus, see Fig. 2b.)

3.4.3. Total creep

The measured total compliance under axial compression is compared to the B3 and *fib* prediction in Fig. 16 and to the FEM simulation with MPS model in Fig. 17. Similarly to the basic creep, the measurements are vertically shifted to match the short-term compliance and are compensated for the total shrinkage.

On the measured time range the agreement is better with *fib* than with B3 model. Comparison with FEM reveals that the model response is almost insensitive to the magnitude of drying shrinkage. With default k_3=30 the drying creep component is approx. twice as high as in the case of the B3 model.

The compliance measured or computed using FEM under eccentric compression is split and presented separately for axial shortening, J^{ε}_{tot}, and bending, J^{κ}_{tot}. The axial compliance was computed as a ratio of the stress-related average deformation, $\varepsilon_\sigma(t)$, divided by the imposed average stress $\bar{\sigma} = F/A$ where $F = -50$ kN is the prescribed load, and A=0.01 m^2 is the cross-sectional area. The deformation $\varepsilon_\sigma(t)$ was obtained as the average deformation of the loaded specimen compensated for the average shrinkage strain (measured on companion specimen without external load).

The compliance in bending was evaluated as $J^{\kappa}_{tot}(t, t') = \kappa(t)I/M$ where I=0.1^4/12 m^4 is the moment of inertia and $M = F \cdot e$ with e being the prescribed eccentricity 16.7 mm. The curvature $\kappa(t)$ was taken as the strain difference measured at the opposite faces of the loaded specimen divided by the distance between the strain gauges (experiment: 0.1 + 2 × 0.015=0.13 m, FEM: 0.1 m).

In Figs. 18 and 19, the compliance is compared to the prediction of the average cross-sectional models (B3, *fib*) and coupled FEM simulation, respectively.

In contrast to the axial compliance, the contribution to the compliance in bending increases with the distance from the centroid. On the beginning of drying the relative humidity in the vicinity of the exposed surface decreases significantly faster than in the center. This relatively fast decrease triggers not only drying creep compliance but, owing to the internal restraint, also shrinkage-induced microcracking which causes additional increase in compliance. Therefore it can be expected that J^{κ}_{tot} will, at least initially, grow faster than J^{ε}_{tot}. The experimental data obtained from the measurements ($J_{tot}^{exp,\ \varepsilon}$, $J_{tot}^{exp,\ \kappa}$) confirm this anticipated behavior.

In the cross-sectional models the evolution of drying creep is entirely governed by the effective thickness and the models do not reflect the nature of loading. For this reason Fig. 18 shows only a single curve for the total compliance of each model considered. The measured axial compliance $J_{tot}^{exp,\ \varepsilon}$ nicely follows the prediction of the B3 model J_{tot}^{B3}. The *fib* prediction evolves initially similarly to B3 but after ≈100 days the creep rate becomes remarkably lower.

In contrast to the cross-sectional models, the FEM simulations make it possible to correctly distinguish the axial and bending compliance. The agreement of the FEM simulation with the experimental data is exceptional. In the current experimental setup the model response is almost insensitive to the magnitude of the drying shrinkage coefficient k_{sh}. Also in the case of eccentric compression, the default value k_3=30 yields approximately twice as high ultimate drying compliance than the B3 model.

Additionally, the model predicts the same value of the ultimate axial and bending compliance. The explanation for this needs to be sought in the value of the exponent p in the differential equation for the microprestress. The available experimental data from the literature indicate that the size-effect decreases with increasing specimen size; however, the original MPS theory with p=2 gives an opposite behavior [13]. The size-effect on drying creep becomes eliminated in the special case when $p = \infty$ [14], which is done here. Since the axial and bending compliance evolve with different rates, the processes possess different characteristic times; however, due to the zero size-effect on drying creep, the ultimate drying compliance in bending and compression become equal.

3.5. Non-symmetrically drying beams

3.5.1. Group I, span 1.75 m, 2.5 m and 3.0 m

The consistency of the measured data and the magnitude of the vertical deflection is illustrated on example of beam #7 from Group I (height 150 mm, span 3 m, drying from top surface) shown in Fig. 20. Every data point in this Figure is the average of two consecutive readings using the digital indicators. The accuracy of this measurement technique is sufficient for the present purpose and the magnitude of the displacement of the five data series is in correct order (the value increases with the distance from the supports). In all Figures in this Section, downward displacement is treated as positive and the values of instantaneous deflections were back-calculated using the density 2300 kg/m^3 and 1-month value of Young's modulus.

Consistency of the measured data allows to present only the deflection at the midspan in the following Figs. 21–24. The blind prediction using FEM is shown by the solid lines and the updated prediction with adjusted shrinkage constant k_{sh} by dashed lines. The color of the lines matches the respective experimental data series.

The influence of the drying shrinkage, drying creep and microcracking on the development of vertical deflection is shown in Fig. 21. The strikingly different behavior of the beams #1–#4 from Group I with identical dimensions and span 2.5 m is a result of different sealing setup. The reference case of entirely sealed beam #2 does not exhibit significant increase after ≈50 days of loading. Yet the comparison with the computational model suggests that the recorded deflection initially substantially overestimated the expected behavior and might be caused by delayed microcracking on the bottom (tensile) face of the beam. As the recorded deflections are in this case relatively small, the observed trends and the drawn conclusions need to be further supported by the experimental data measured on the other two identical specimens by DIC (unavailable at the time of writing).

Already after several days of loading the symmetrically drying beam #4 from Group I (purple color) deflects significantly more than the reference beam. Interestingly, the difference remains almost constant

during the first month after which it starts increasing. After one year the deflection reaches 1.965 mm which is 72% more than the reference (sealed) case (1.140 mm). Since the drying conditions are symmetric, the drying shrinkage per se does not produce any curvature and deflection. The origin must be sought in highly nonuniform distribution of self-equilibrated stresses over the height which produces microcracking and causes higher overall compliance. The subsequent increase in deflection is due to the drying creep. To achieve a better transparency of the results, the increase in deflection due to drying is depicted in Fig. 22.

The results of the FEM simulations confirm this assumption. During the first few days, the response of the original blind prediction (shown in solid line) does not exhibit any sudden increase in deflection and almost coincides with the reference basic creep behavior. On the other hand, twofold increase of the drying shrinkage constant amplifies the stress gradient which consequently leads to microcracking and as a result produces higher compliance in bending.

The measured as well as the predicted deflection of the beams subjected to non-symmetric drying (#2 and #3 in Group I) can be perceived as surprising or at least as interesting. Firstly, the improved prediction matches the experimental data almost perfectly, both in terms of the evolution and magnitude and both for the specimen drying from the top surface (shown in red color) and bottom surface (black color). Secondly, what becomes notable when plotted in semi-logarithmic scale, the evolution has two peaks, the first after ≈2 months and the second one after 3 years (at the present moment only prediction). Finally, in terms of deflection, the non-symmetric drying represents the predominant factor causing 300% increase in deflection compared to the reference sealed specimen. Fig. 22 documents that up to ≈100 days the deflection produced by non-symmetric drying only evolves very similarly for both directions of drying. As confirmed by the numerical simulations, the beam drying downwards deflects slightly less due to the curvature induced by the gradient of drying shrinkage. This can be explained by more pronounced microcracking; the effect of bending and drying shrinkage add at bottom fibers which results into bigger tension and thus more severe damage. The results of the finite element simulations are illustrated in Fig. 23 which shows the distribution of the normal stress σ_x after 1 year of drying. The computational model was a symmetric half of the beams.

The evolution of vertical deflection of the beams drying from the top surface with height ranging from 50 mm to 200 mm is compared in Fig. 24. It needs to be emphasized that the deflection due to drying is driven not only by the gradient of drying shrinkage strain over the height, but depends also on the span which varies in the individual cases. The predicted evolution of deflection shows that the two peaks are present in all investigated cases. The position of the first, more subtle peak ranges from 10 days (50 mm) to 300 days (200 mm), followed by more dominant second peak between 300 days (50 mm) and 5000 days (200 mm). The drying effects stop after the period ranging from 5000 days (h=50 mm) to 50,000 days (h=200 mm). Afterwards, the deflection rate is driven by the creep at lower level of relative humidity which is less than the basic creep.

Comparison of the experimental data to the FEM prediction suggests that the excellent agreement obtained for the beams with 100 mm height was merely a coincidence. The improved prediction (dashed lines) considerably overestimates the deflection of the smallest specimen (#5, 50 mm), however, this specimen might not be perfectly representative due to the maximum aggregate size. In the case of 150 mm and 200 mm deep beams the initial trend is captured correctly up to the position of the first peak. The experimental data then continue growing while the simulations predict the opposite tendency.

3.5.2. Group II, span 2 m

The measured deflections at the midspan of beams with 2-m span (Group II) are shown in linear scale in Fig. 25. The points in this Figure correspond to the values determined using the digital indicators while the solid lines were automatically recorded with the displacement sensors. The purple color distinguishes the specimens without external loads in the first month. It is worth mentioning that the two measurement techniques prove exceptional agreement. The wobbly trend (also apparent in the case of 50 mm and 100 mm deep beams drying non-symmetrically, see Fig. 24), is not caused by insufficient accuracy but instead is a consequence of uncontrolled fluctuations in the ambient relative humidity.

The results of numerical simulations shown in Fig. 26 correspond to the beams with permanent external loading. The improved FEM prediction (shown in orange and grey color) does not capture the experimental data as perfectly as in the case of the specimens from Group I although the height is the same. The influence of microcracking on vertical deflection of beams drying either from the top or from the bottom surface becomes even more pronounced.

Comparison between the measured and computed response to loading and unloading is shown in Fig. 27 for one month and in Fig. 28 for one year. The data in these Figures were obtained under the assumption that the short-term visco-elastic behavior outweighs the long-term effects which can be for this purpose neglected. To prevent oscillations in vertical deflection caused by fluctuating ambient relative humidity, the loaded (or unloaded) beam had to be related to the corresponding continuously loaded beam.

In the Figures, the noisy lines are the experimental measurements, the smooth lines were obtained from the numerical simulations. Solid lines represent the response due to loading and the dashed lines denote the unloading; the colors match the sealing setup like in the preceding Figures. The blind prediction is presented in Figs. 27a and 28a while the improved prediction in Figs. 27b and 28b.

The order of the curves reflects the stiffness at the time of loading or unloading. Both the experiment and the simulation confirm the expected behavior: the sealed beams (in blue color) have the highest stiffness followed by the specimens drying from the top surface. In the beams drying from the bottom surface the tensile stress due to bending meets with the tension caused by drying shrinkage and together produce the most extensive microcracking and the highest compliance.

However, as demonstrated in Fig. 27, the measured difference between the drying and sealed specimens is much bigger than what predicts the simulation. The results of FEM simulations also prove that the bending stiffness is very sensitive to the magnitude of drying shrinkage. With the improved prediction (twofold magnitude of k_{sh}), the differences between the drying setup start becoming more pronounced. Yet, the model as well as the experiment almost do not distinguish between loading and unloading (dashed vs. solid lines).

The response to loading and unloading approx. 1 year after the beginning of the experiment is shown in Fig. 28. On contrary to the previous case, the sealed specimens are captured perfectly, however, the difference between the drying beams still remains underestimated even with the improved prediction. With the blind prediction the behavior of the drying beams unifies and so does the response to loading and unloading.

4. Conclusions

This paper summarizes a new experimental study focused on a time-dependent behavior of normal-strength structural concrete (f_{cm}=37 MPa) with $w/c = 0.49$. The data in this paper cover the first year of the experiment whose duration will exceed 3 years. A special attention is paid to the interaction of shrinkage, creep and microcracking caused by symmetric and non-symmetric drying. The cornerstone of the experimental program consists of a large set of unreinforced beams with different sealing setup, height from 50 mm to 200 mm and span from 1750 mm to 3000 mm. This key experiment is supplemented with standard short-term measurements as well as long-term investigation of creep, shrinkage, and weight loss. The measured data is compared to the blind prediction with the modified MPS material model and B3/B4/*fib* MC 2010 models.

The resulting experimental database is suitable for calibration, validation and further development of the advanced constitutive models for creep and shrinkage operating on the material-point level. The

complete experimental data published in this paper and other supplementary materials are available online at Mendeley Data [15]. The main observations can be summarized as follows.

1. Comprehensive design of experiments yielded consistent data for autogenous shrinkage, drying shrinkage, basic and drying creep for concrete specimens and beams.
2. The short-term creep experiment (loading duration 30 s–1 h) proves the superior performance of the B3 model for concrete creep. At this time range the *fib* formula gives almost constant value of the compliance function. The experiments testify that the Young modulus corresponds to the inverse of compliance function for $t - t' \approx 0.002$ days (3 min).
3. The *fib* recommendation on moisture transport which uses the BaÅ¾ant-Najjar model gives very accurate prediction of the drying kinetics.
4. Even though the applied blended cement CEM II 32.5 R B—S is designated as rapid hardening, the high slag content 29% causes that the development of strength and stiffness is captured more accurately with *fib* formula for the cement with normal strength gain, CEM 32.5 N.
5. Drying creep measured on prisms loaded in eccentric compression and subject to symmetric drying evolves faster in bending than in compression and corresponds to FEM results. This is due to nonuniform drying which significantly increases drying compliance in the vicinity of drying surface which increases bending compliance more than axial compliance.
6. Micro-cracking caused by drying shrinkage has a considerable impact on stiffness in bending.
7. The numerical model predicts that the evolution of vertical deflection of beams subjected to drying from one side only has two extremes.
8. The overall performance of the modified MPS model (with zero size effect on drying creep) can be evaluated as exceptional. The improved prediction which differed from the blind prediction only in the magnitude of the drying shrinkage constant yielded very good agreement with most of the experiments.

CRediT authorship contribution statement

P. Havlásek: Conceptualization, Methodology, Formal analysis, Data Curation, Investigation, Writing - Original Draft, Visualization, Supervision, **V. Šmilauer**: Conceptualization, Investigation, Data Curation, Writing - Review & Editing, **L. Dohnalová**: Investigation, **R. Sovják**: Investigation.

Declaration of competing interest

The authors declare that they have no known competing financial interests or personal relationships that could have appeared to influence the work reported in this paper.

Acknowledgment

Financial support for this work was provided by the Czech Science Foundation (GA ČR), project number 19-20666S (Shrinkage-induced deformations and microcracking in structural concrete - monitoring, modeling and identification).

A special acknowledgment goes to the personnel of the Department of Mechanics and Experimental Center who got involved in preparation of the experiment and measurement, especially M. Lepš, P. Reiterman, J. Litoš, Z. Prošek, J. Klingerová, J. Trejbal, O. Zobal and P. Horák. The authors would like to thank Dr. Martin Vavro from the Czech Academy of Sciences for classifying the aggregates in the concrete mixture.

References

[1] Z. Bažant, M. Jirásek, Creep and Hygrothermal Effects in Concrete Structures, Springer Netherlands, 2018.
[2] A. Neville, Properties of Concrete, Wiley, 2011.
[3] Z. Bažant, S. Baweja, Creep and Shrinkage Prediction Model for Analysis and Design of Concrete Structures: Model B3, Adam Neville Symposium, Creep and Shrinkage - Structural Design Effects, 2000.
[4] O. Coussy, Poromechanics, John Wiley & Sons, Ltd, 2004.
[5] A. Aili, M. Vandamme, J.-M. Torrenti, B. Masson, A viscoelastic poromechanical model for shrinkage and creep of concrete, Cem. Concr. Res. 129 (2020) 105970.
[6] P. Yu, Y. Duan, Q. Fan, S. Tang, Improved mps model for concrete creep under variable humidity and temperature, Constr. Build. Mater. 243 (2020) 118183.
[7] S. Rahimi-Aghdam, Z.P. Bažant, G. Cusatis, Extended microprestress-solidification theory for long-term creep with diffusion size effect in concrete at variable environment, Journal of Engineering Mechanics 145 (2) (2019) 04018131.
[8] S. Liang, Y. Wei, Methodology of obtaining intrinsic creep property of concrete by flexural deflection test, Cem. Concr. Compos. 97 (2019) 288–299.
[9] H. Huang, R. Garcia, S.-S. Huang, M. Guadagnini, K. Pilakoutas, A practical creep model for concrete elements under eccentric compression, Materials and structures 52 (2019).
[10] RILEM, Technical Committee TC-242-MDC (Z.P. Bažant, chair), "Model B4 for creep, drying shrinkage and autogenous shrinkage of normal and high-strength concretes with multi-decade applicability.,", Materials and Structures 48 (2015) 753–770.
[11] Fédération Internationale du Béton, *Model Code 2010*. No. vol. 65 in fib Bulletin, International Federation for Structural Concrete (fib), 2012.
[12] Z.P. Bažant, A.P. Hauggaard, S. Baweja, F.J. Ulm, Microprestress solidification theory for concrete creep. I: aging and drying effects, J. Eng. Mech. 123 (1997) 1188–1194.
[13] Z. Bažant, P. Havlásek, M. Jirásek, Microprestress-solidification theory: Modeling of size effect on drying creep, in: N. Bicanic, H. Mang, G. Meschke, R. de Borst (Eds.), Computational Modelling of Concrete Structures, EH Leiden, The Netherlands, 2014, pp. 749–758. CRC Press/Balkema.
[14] P. Havlásek, Creep and Shrinkage of Concrete Subjected to Variable Environmental Conditions, PhD. Thesis. Czech Technical University in Prague, 2014.
[15] P. Havlásek and V. Šmilauer, "Data to: Shrinkage-induced Deformations and Creep of Structural Concrete: 1-year Measurements and Numerical Prediction." https://doi.org/10.17632/6ngycd6dzx.1.
[16] J. Godány, T. Jandová, M. Poňavič, K. Rýda, J. Buda, P. Rambousek, I. Knésl, Š. Mrázová, J. Starý, Update of the Passporting of Natural Aggregate Quarries of the Czech Republic (in Czech), 2018.
[17] P. Koutník, P. Antoš, P. Hájková, P. Martinec, B. Antošová, P. Ryšánek, J. Pacina, J. Šancer, J. Ščučka, V. Bruna, Stones, Sandpits and Limestone Quarries in the Czech Republic, 2015.
[18] BS EN 12390-13:2013, Testing Hardened Concrete Part 13: Determination of Secant Modulus of Elasticity in Compression. BSI British Standards Publication, 2013.
[19] BS EN 12390-3:2009, Testing Hardened Concrete Part 3: Compressive Strength of Test Specimens. BSI British Standards Publication, 2011.
[20] BS EN 197-1:2011 Cement, Part 1: Composition, Specifications and Conformity Criteria for Common Cements Concrete - Specification, Performance, Production and Conformity. BSI British Standards, Publication, 2011.
[21] A.H. Bryant, C. Vadhanavikkit, Creep, shrinkage-size, and age at loading effects, ACI Mater. J. 84 (1987) 117–123.
[22] Z.P. Bažant, L.J. Najjar, Nonlinear water diffusion in nonsaturated concrete, Mater. Struct. 5 (1972) 3–20.
[23] R. Sovják, P. Havlásek, J. Vítek, Long-term behavior of concrete slabs prestressed with CFRP rebars subjected to four-point bending, Constr. Build. Mater. 188 (2018) 781–792.
[24] V. Šmilauer, P. Havlásek, T. Gasch, A. Delaplace, D.E.-M. Bouhjiti, F. Benboudjema, M. Briffaut, F. Kanavaris, M. Azenha, Hygro-mechanical modeling of restrained ring test: COST TU1404 benchmark, Constr. Build. Mater. 229 (2019) 116543.
[25] V. Nežerka, P. Havlásek, J. Trejbal, Mitigating inclusion-induced shrinkage cracking in cementitious composites by incorporating recycled concrete fines, Constr. Build. Mater. 248 (2020) 118673.
[26] R. de Borst, J.J.C. Remmers, A. Needleman, M.-A. Abellan, Discrete vs smeared crack models for concrete fracture: bridging the gap, Int. J. Numer. Anal. Methods Geomech. 28 (7–8) (2004) 583–607.

[27] Z.P. Bažant, B.H. Oh, Crack band theory for fracture of concrete, Mater. Constr. 16 (May 1983) 155–177.
[28] B. Patzák, OOFEM home page. http://www.oofem.org, 2000.
[29] B. Patzák, OOFEM - an object-oriented simulation tool for advanced modeling of materials and structures, Acta Polytechnica 52 (6) (2012) 59–66.
[30] K. Lee, H. Lee, S. Lee, G. Kim, Autogenous shrinkage of concrete containing granulated blast-furnace slag, Cem. Concr. Res. 36 (7) (2006) 1279–1285.
[31] Z. Liu, W. Hansen, Aggregate and slag cement effects on autogenous shrinkage in cementitious materials, Constr. Build. Mater. 121 (2016) 429–436.
[32] E. Tazawa, S. Miyazawa, Influence of cement and admixture on autogenous shrinkage of cement paste, Cem. Concr. Res. 25 (2) (1995) 281–287.
[33] Q. Wang, P. Yan, J. Yang, B. Zhang, Influence of steel slag on mechanical properties and durability of concrete, Constr. Build. Mater. 47 (2013) 1414–1420.
[34] M. Shariq, J. Prasad, H. Abbas, Creep and drying shrinkage of concrete containing ggbfs, Cem. Concr. Compos. 68 (2016) 35–45.
[35] J. Yuan, W. Lindquist, D. Darwin, J. Browning, Effect of slag cement on drying shrinkage of concrete, ACI Mater. J. 112 (2) (2015) 267–276.